Materials and Design 171 (2019) 107703

Contents lists available at ScienceDirect

Materials and Design

journal homepage: www.elsevier.com/locate/matdes

Branching of {110) twin boundaries in five-layered Ni-Mn-Ga bent single crystals

R. Chulist [a,*], L. Straka [b], H. Seiner [c], A. Sozinov [d], N. Schell [e], T. Tokarski [f]

[a] Institute of Metallurgy and Materials Science, Polish Academy of Sciences, 30-059 Krakow, Poland
[b] Institute of Physics of the Czech Academy of Sciences, Na Slovance 1999/2, 182 21 Praha 8, Czech Republic
[c] Institute of Thermomechanics, Czech Academy of Sciences, Dolejškova 5, 18200 Prague, Czech Republic
[d] Material Physics Laboratory, Lappeenranta University of Technology, Laitaatsillantie 3, 57170 Savonlinna, Finland
[e] Institute of Materials Research, Helmholtz-Zentrum Geesthacht, Max-Planck-Str. 1, D-21502 Geesthacht, Germany
[f] AGH University of Science and Technology, Academic Centre for Materials and Nanotechnology, Mickiewicza 30, 30-059 Krakow, Poland

HIGHLIGHTS

- Twin tapering and elastic change of lattice parameters cause pseudoelastic effect with a large bending angle of 129°.
- The plastic-elastic response is explained by an *equilibrium between distance of piled-up dislocations and twinning stress.*
- Bending refines {110) twins in order to maintain the compatibility along the tapered {101) twins.

GRAPHICAL ABSTRACT

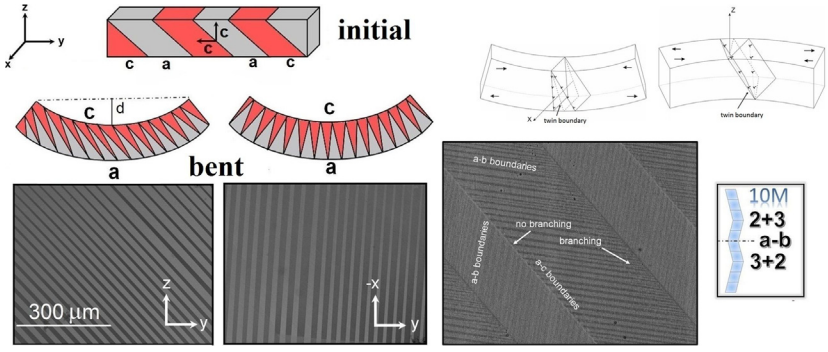

ARTICLE INFO

Article history:
Received 1 December 2018
Received in revised form 11 March 2019
Accepted 12 March 2019
Available online 13 March 2019

Keywords:
NiMnGa
Bending
Twinning
Interfacial misfit
Continuum mechanics

ABSTRACT

Two bending tests around two perpendicular axes were applied to 10M Ni-Mn-Ga single crystals with five-layered modulated structure. The crystal structure and microstructure evolution were examined using synchrotron radiation and electron backscatter diffraction, respectively. The bend stress results in pseudoelasto-plastic strain due to {101) twins tapering. A close examination of the microstructure reveals an additional pattern indicating microstructural changes in the form of {110) twins. As bending proceeds the {110) twins branch undergoing a significant twin refinement. Additionally, an elastic change of lattice parameters is confirmed yielding a higher total pseudoelastic strain. Unloading restores the initial twin configuration removing a large amount of the {110) twin boundaries, however, this process is followed by incomplete recovery since the samples do not retain its original shape entirely. The paper underlines the differences in mechanism for bending around two perpendicular axes explaining the amount of strain observed under pseudoelastic deformation. Additionally, the results are discussed with respect to minimization of elastic energy due to twin refinement and branching as well as mobility of the {101) and {110) twin boundaries.

* Corresponding author.
E-mail address: r.chulist@imim.pl (R. Chulist).

https://doi.org/10.1016/j.matdes.2019.107703

1. Introduction

Extremely low twining stress is an outstanding property of Ni-Mn-Ga magnetic shape memory (MSM) single crystals [1–8]. Consequently, easy twin boundary motion leads to reorientation of variants resulting in high permanent strains which can be obtained by a mechanical loading or magnetic field. The applied stress between 0.01 and 1 MPa or the so-called magnetic field-induced reorientation (MIR) [9] give rise to a strain up to 12% [10–16].

However, so far the reason for the very high mobility of type I and type II twin boundaries in 10M Ni-Mn-Ga single crystals is not completely clear. One of the possible explanations is given by Seiner et al. where the high mobility of twin boundaries in 10M Ni-Mn-Ga structure is related with a complex crystal structure of 10M martensite and the order of compatibility (coherence) between the twinned variants [17]. The suggested model considered the modulated monoclinic 10M structure with a very small difference in the *a* and *b* lattice parameters and the resulting microstructures to be the reasons for high mobility of type II twin boundaries. This correlates very well with other reports given by Faran et al. who show some energy barriers, and related with that microstructural elements, the width of which is consistent with distribution of *a*-*b* lamination [18–20]. Thus, it seems that the {110) twins (further referred to as *a*-*b* twins) are strongly related with high mobility of {101) twin boundaries [21–23].

Extremely low twinning stress and the ability for abundant tapering of twin planes also enable the whole spectrum of super or pseudoelastic effects in Ni-Mn-Ga system. For clear distinction between pseudoelasticity and superelasticity see [24]. Depending on the twin boundary configuration (parallel, perpendicular or mixed), different effects can be observed [25–42]. For instance Müllner and Kostorz reported that an interaction of crossing twin boundaries can result in a significant pseudoelastic and magnetoelastic effect which may result in magneto-elasticity, magneto-plasticity, and magnetically induced pseudoelasticity. On the other hand, by means of creating fine parallel twins improved fatigue properties can be obtained [26,30]. Thus, the so-called twin domain engineering allows to achieve a wide variant of effects. It is based on large deformation which can be induced by magnetic and/or mechanical fields having potential application in actuation, medical and aerospace technologies. Among the reported works mostly superelastic effect is studied using compression-tension loading. However, bending as another mode of operation of ferromagnetic SMAs opens a number of opportunities for original design of bending actuators using the coupling between magneto, thermal and mechanical properties [43].

In this work a simple pure bending (two-point bending) around two different axes was applied to Ni-Mn-Ga 10M single crystals. As the bending stress increases the twin planes start deviating from the {101) plane (the so-called *a*-*c* twins). The {) notation used means that

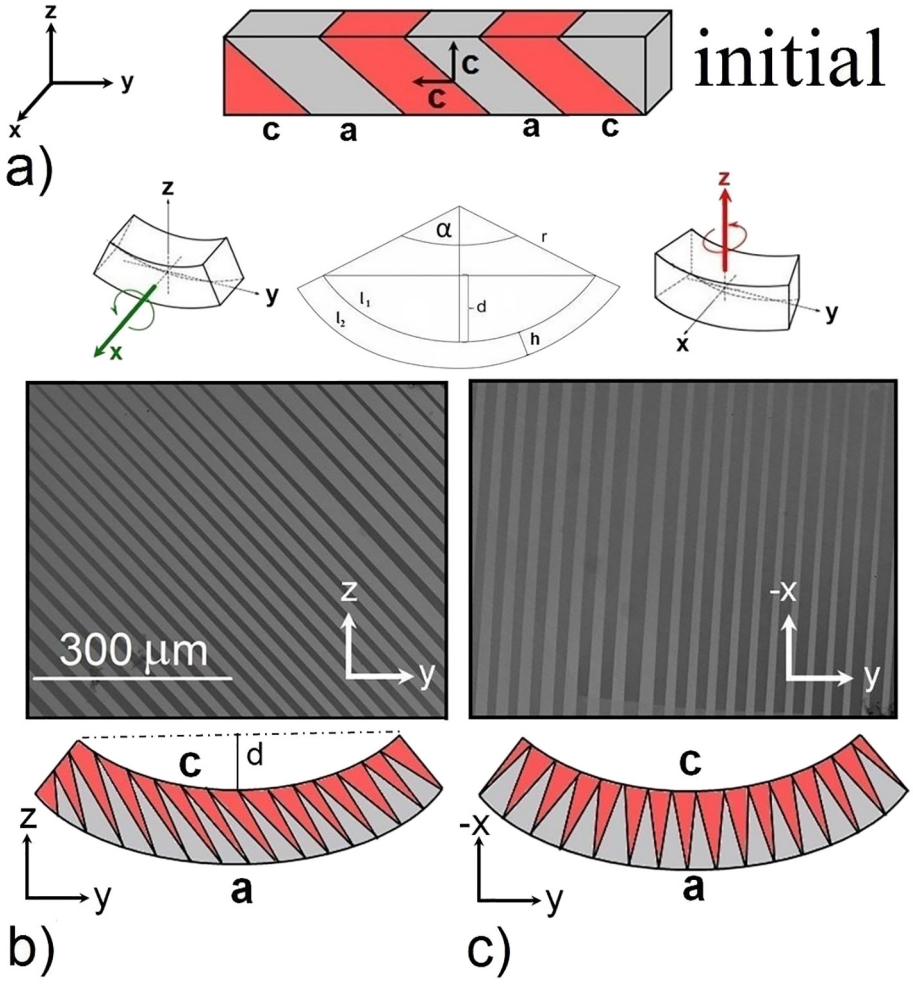

Fig. 1. A schematic sketch of the initial sample (a) and BSE images taken on two perpendicular surfaces for bent single crystals around x (b) and z-axis (c). Depending on the bent axis tapering of *a*-*c* boundaries on different surfaces can be seen. Illustrations below represent schematic sketches of the bent samples indicating the exchange of *a* (or *b*) and *c* lattice axes at the inner and outer bending curvature. The bending angle is indicated by α whereas the inner bending deflection is indicted by *d*. l_1 and l_2 stand for inner and outer lengths, respectively, while h for sample thickness and r for bending radius.

the first two indices may be permuted whereas the third index is fixed. The twin plane deviation mechanism is associated with generation of piled-up dislocations arrayed on successive twin planes [44]. However, up to now this mechanism was limited to bending around only one axis which forms tapering of the twin traces lying under 45° on the YZ projection as it is shown in Fig. 1a, see also [45]. More complex configurations are studied both experimentally and theoretically by Ganor et al. showing zig-zag twins and helical martensitic transformations [46].

Nevertheless, the pure bending around the z-axis which results in deviation of twin plane on the XY projection (twin trace parallel close to the ⟨100⟩ direction, Fig. 1b) was not considered before. Moreover, the role of {110) boundaries was disregarded with respect to tapered twin boundary compatibility. In this work using synchrotron and electron backscatter diffraction (EBSD) techniques we experimentally confirm the existence of {110) *a*-*b* boundaries showing their significant refinement in order to facilitate the compatibility along the tapered {101) twins (further referred to as *a*-*c* or *b*-*c* twins). The obtained results are consistent with a predicted microstructure showing a significant refinement of *a*-*b* twins near the macro-twin interface.

2. Method

In order to investigate the bending response, single crystal samples with the composition of $Ni_{50.2}Mn_{28.3}Ga_{21.5}$ (±0.5 at.%) and dimensions of 0.75 × 2.3 × 20 mm^3 were used. The single crystals were obtained from AdaptaMat Ltd. The orientation of samples was ⟨100⟩{001} expressed in the so-called cubic coordinates [47-52]. The samples were mechanically polished using silicon carbide paper up to 7000 grit and electropolished with 10 vol% $HClO_4$ in ethanol at 0 °C and at 40 V polishing voltage for 7 s. All BSE images and EBSD maps (except the unbent sample imaged in Fig. 3a) were collected at the stress state which created the bending angle α equal to 129° (bending deflection of 5 mm, see Fig. 1a).

The bent and unbent samples were also measured by diffraction of high-energy synchrotron radiation (87.1 keV) in transmission geometry using the HZG materials science beamline P07B at DESY in Hamburg, Germany. A screw-based compression device with only displacement control was used to bent the samples for EBSD and synchrotron measurements. The same loadings with an Instron testing machine were conducted to record load-displacement curves. Additionally, the strain state was defined by bending deflection given by a distance *d*, Fig. 1a. The sample was transmitted with synchrotron radiation with a beam size of 0.7 × 0.7 mm along the z-direction at different bent conditions starting with initial unbent sample and gradually increasing the bending deflection up to the distance of 5 mm. Such an arrangement allowed to control the distribution of the so-called *a* and *b* martensitic variants. The crystal structure determined by synchrotron X-ray diffraction at room temperature is 10M martensite with the following lattice parameters: $a = 0.5972$ nm, $b = 0.5947$ nm, $c = 0.5583$ nm, $\gamma = 90.37°$.

Investigations of microstructure and orientation were performed after loading using a FEI Quanta 3D SEM and the TSL system. In order to determine a very small difference between *a* and *b* lattice parameters a dedicated software based on the extremely small changes in Hough space was developed. It is based on indexing and comparing only small regions in Hough space. For distinction between the *a* and *b* lattice parameters only the area in close vicinity to (110) poles was analyzed. It has to be mentioned that no commercially available EBSD software is able to distinguish between the *a* and *b*-axes in the 10M Ni-Mn-Ga. Only the so-called *a*-*c* and modulation boundaries have been detected with an automatic EBSD software so far [53-62]. Additionally, a special channeling contrast condition was used to image the so-called modulation and *a*-*b* boundaries using BSE in SEM. To index the Kikuchi lines obtained from EBSD scans the monoclinic long-periodic modulated structure was used. However, for easy comparison with previous reports and to keep the commonly accepted convention, all results and the discussion are given in the so-called cubic coordinates.

3. Results and discussions

As a starting material, samples with fine parallel twins of type I with a size of about 40 μm and only two variants with respect to *c*-axis were chosen. Diffraction of synchrotron radiation showed that only one modulation direction in each variant was present, Fig. 2. Thus, no modulation {100) twins were detected in the initial state of the sample. The same observation was confirmed by BSE imaging and EBSD in the SEM. Going deeper into the microstructure the initial distribution of *a*-*b* lamination was studied. Only small amount of *a*-*b* twins was detected with BSE imaging as portrayed in Fig. 3a. A similar observation was made employing synchrotron X-ray diffraction in transmission geometry, Fig. 2a and b. This clearly shows that the initial state of the sample was dominated by two variants with the common *b*-axis parallel to z direction, however, some minor variants with *a*-axis parallel to z direction were present as well. Such single crystals were subjected to bend

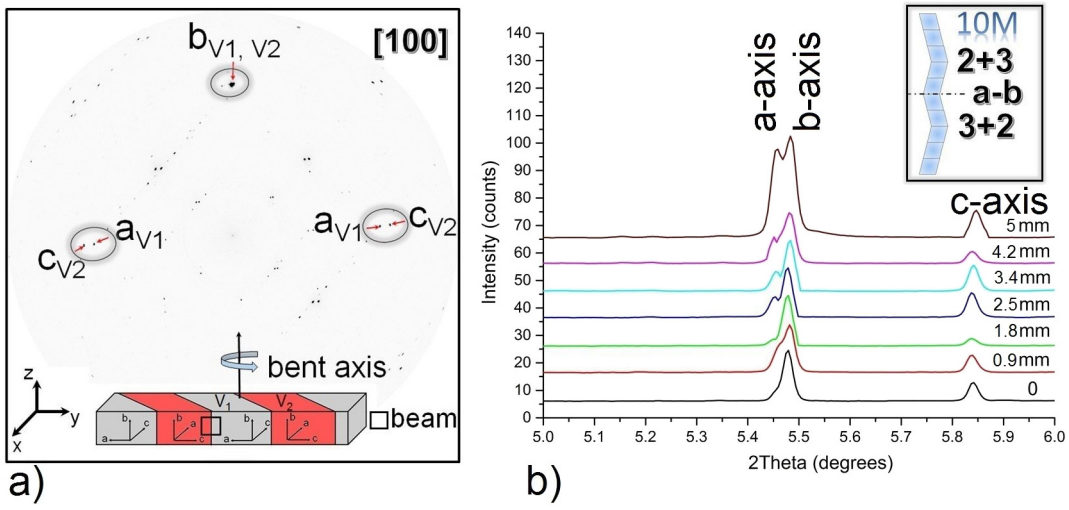

Fig. 2. Initial unbent sample transmitted with synchrotron radiation and diffraction pattern showing predominantly two-variant structure with common *b*-axis and interchanging *a*-*c* axes (a). Integrated X-ray synchrotron diffractions illustrating the lattice parameters as a function of bending deflection (see Fig. 1) (b). Top-right insert illustrates the concept of *a*-*b* boundaries as inverting stacking fault for 10M martensite [16].

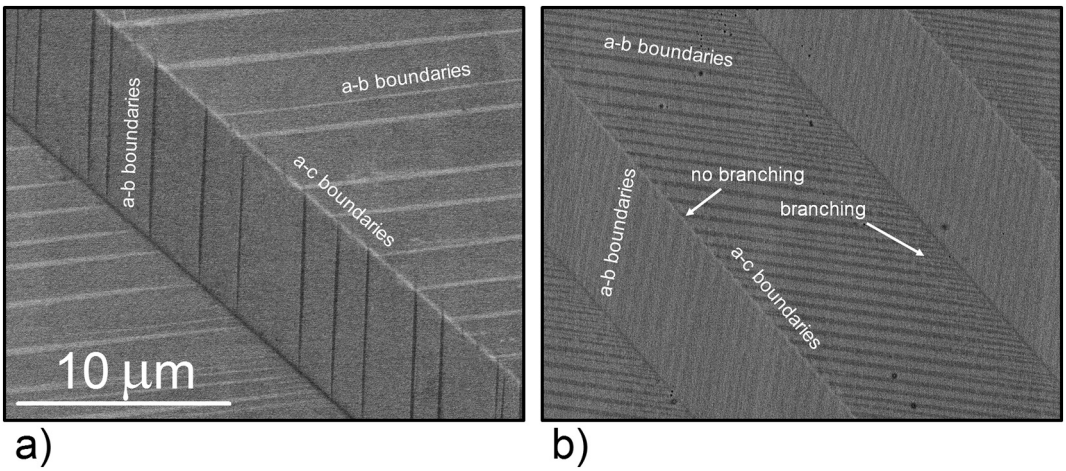

Fig. 3. BSE images show *a*-*b* and *a*-*c* twins in the unbent (a) and bent (b) single crystals ($d = 5$ mm) taken on the YZ projection.

testing. The mechanical response of the sample is showed in Fig. 4. Before the test, the sample was in slightly bent state in order to maintain the sample in place. After some elastic deformation almost linear response of the sample is observed. Upon unloading a similar loading curve with a hysteresis is detected. The second run reproduces the loading-unloading behavior exhibiting the same hysteresis. As the sample contacts the anvils of the machine only at two points the stress distribution was calculating using a finite element methods. The calculations were performed for two states employing Von Mises stress criteria and elastic moduli from [63]. The first stress state was modeled using a force of 0.4 N which corresponds to point 1 in Fig. 4 and the latter one for a load of 1 N related to point 2. Both states correspond quite well to two cases discussed in the paper i.e. bending with d ≈ 3 mm and a situation when the stress is released, Fig. 5.

As deformation proceeded the tapering of twin boundaries began. The material response was symmetric with an equal distribution of twins along the whole sample. Bending around the x-axis rotates the *a*-*c* and *a*-*b* boundaries around the same axis changing also their distribution which can be clearly seen in Fig. 3. A schematic sketch of the bending mechanism is given in Fig. 1, where the compressive side is dominated by the variant with the *c*-axis (shortest lattice parameter)

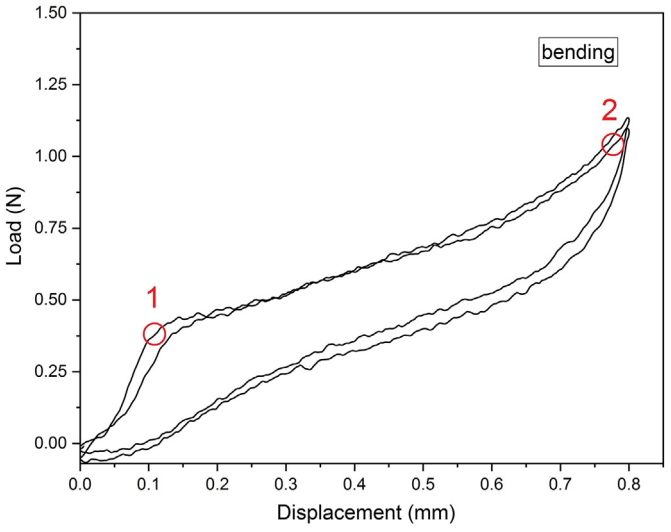

Fig. 4. The load-displacement curve of the two-point bending test performed for two cycles. The red circles indicate the forces used for stress distribution calculations. (For interpretation of the references to colour in this figure legend, the reader is referred to the web version of this article.)

parallel to the sample longest edge while the tensile side by the variant with the longest lattice parameters (*a*-axes) along the sample longest edge. Fig. 1 shows wedge-like structures on two different projections: YZ and XY for single crystals bent around x and z-axes, respectively. Another schematic diagram replicated after Otsuka et al. is demonstrated in Fig. 6a. It shows twinning dislocations introduced on twinning planes which form steps in order to create wedge-like twin boundaries on the YZ projection. A similar dislocation mechanism is proposed in Fig. 6b to explain the wedge-like structure obtained on the XY projection.

However, unlike the bending around the z-axis, where the piled-up dislocations arrayed on successive twin planes have pure edge character, in this case curved dislocations with a screw component are introduced to taper twin boundaries on the XY plane. Using the equations given below the maximum bending angle α can be calculated. For the given sample geometry and lattice parameters (for element description see Fig. 1) α and d were determined to be 97.7° and 3.9 mm, respectively.

$$\alpha = \frac{360 l_1}{2\pi r}, \tag{1}$$

where

$$r = \frac{d l_1}{l_2 - l_1} \tag{2}$$

These values are slightly lower than those obtained experimentally (129° and 5 mm) indicating some additional mechanism for superelastic strain. Analyzing the lattice parameters under bending with x-ray synchrotron diffraction a significant change of *a* and *c* lattice parameters was found. The concomitant shortening of *c*-axis and elongation of the a-axis give an additional elastic strain effect of about 0.9%. Thus, to estimate the total superelastic strain not only tapering of twin boundaries resulting in exchange of *a* and *c*-axes should be taken into account but also elastic properties of the material.

Using equations given in [31,44] the repulsive force per unit length between pure edge dislocations due to elastic interaction for the tapered twins can be determined. This repulsive force can be treated as the origin for restoring the initial unbent configuration. However, as observed experimentally, even if the bending stress is released completely the samples do not recover fully the initial straight shape. It seems that the reason for that is the equilibrium between the distance of the piled-up dislocations and twinning stress. If the restoring stress (repulsive force) is smaller than the twinning stress of type I boundaries the shape recovery is suspended. For the studied samples the α angle at which the above mentioned equilibrium is achieved was calculated to

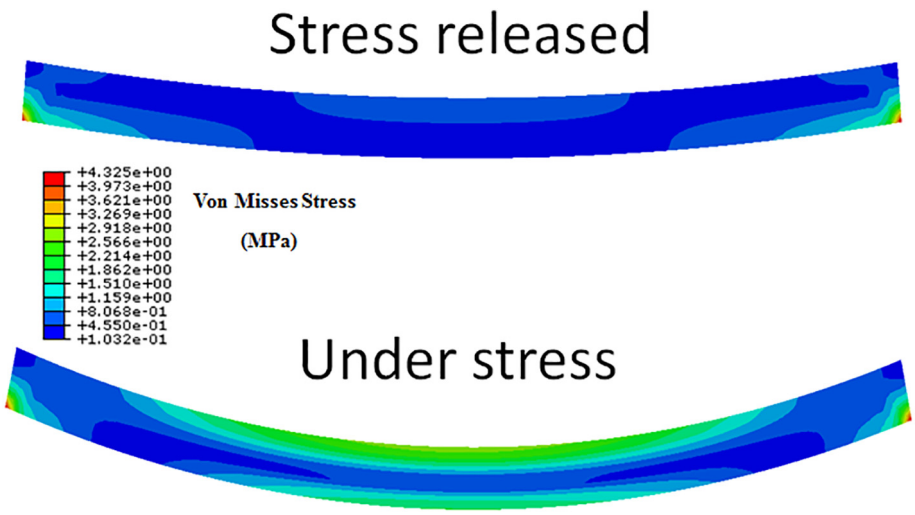

Fig. 5. Stress distribution of the bent sample after application of 0.4 N and 1 N using finite element method and Von Mises stress criteria.

be about 30° [31,44] being in a good agreement with experimental observation. This also indicates that due to a very low twinning stress which is obtained in 10M martensite bending causes rather a mixed response of the material i.e. pseudoelasto-plastic strain. The obtained angles correspond also very well with the stress distribution modeled by finite element method since stresses of about 0.5 MPa are detected in the center part of the sample at the very early deformation stage indicating an equilibrium state.

Studying the mechanism of superelastic strain tapering of {101} twin boundaries was considered so far. These twins, tapered on the YZ and XY projections, are prominently indicated and clearly visible in the BSE and EBSD mode in SEM, Fig. 1. However, a closer look with a higher magnification revealed an additional pattern in-between the {101} twin boundaries (*a*-*c*), Fig. 3. These variants exhibiting a significantly lower contrast are *a*-*b* or {110} twins. They are only visible at specific diffraction conditions in BSE mode. Any bright to dark contrast change seen in Figs. 3 and 7 is related to a change of staking fault from (32) to (23) sequence according to Zhdanov notation creating a mirror plane (a/b boundary) schematically illustrated in Fig. 2. As the bending stress increases an increased number of *a*-*b* boundaries can be observed. It is evident in Fig. 2 where an increasing intensity of the a-axis taken from the upper part of diffraction pattern is observed. The same observation can be made in Fig. 3b or Fig. 7 where a much dense contribution of *a*-*b* twins is revealed. Moreover, a characteristic branching of *a*-*b* twins is observed [64]. Interestingly, the *a*-*b* twins branched only on some *a*-*c* twin boundaries, Fig. 3b and Fig. 7d. Since the conventional EBSD software did not distinguish any differences in these lamellae, Fig. 7c, a dedicated software was applied to index the additional pattern. Taking into account an extremely small differences between *a* and *b* lattice parameters (~0.4%) a specific scan in Hough space focused only on the {110} planes has revealed {110} twinning with a misorientation of about 90.3° around the ⟨001⟩ axis, Fig. 7d.

An extensive twinning of the *a*-*b* variants was also confirmed by X-ray synchrotron diffraction. Diffraction taken from a large sample volume in transmission geometry has clearly indicated that the initial samples show mainly two variants schematically demonstrated in Fig. 2a. With increasing bending curvature more variants with *a*-axis parallel to the z direction show up in the diffraction pattern, Fig. 2b. It has to be mentioned here that a higher intensity of *a*-axis which is integrated in the form of 2θ/Intensity graph in Fig. 2b is coming from the upper part of the 2D diffraction pattern. It strongly confirms the appearance of *a*-*b* lamination. Fig. 2 refers to the sample bent around the z-axis. Similar results were obtained for bending around the x-direction, where *a*-*b* lamination was also distinguished.

The substantial refinement of the *a*-*b* twinning in the bent samples can be, from the theoretical point of view, explained based on two different mechanisms. The first one follows from the compatibility conditions at the *a*-*c* twin planes, the second one then from the characteristic length of the *a*-*b* twins, which significantly differs between the bent and the unbent samples. As described in detail in [17] the *a*-*b* twin planes can cross compatibly with the type I *a*-*c* interfaces running exactly along the {110} planes. The term compatible crossing

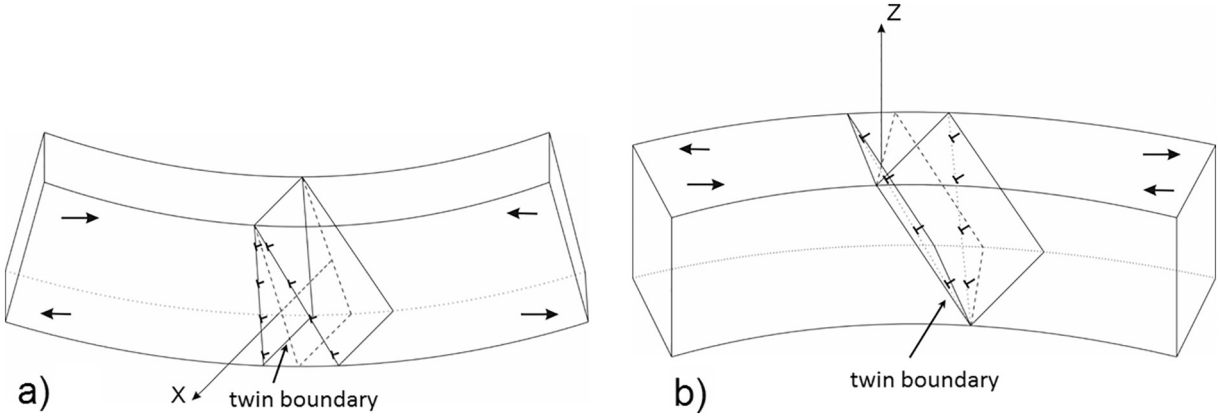

Fig. 6. Mechanism of twin boundary tapering with regard to twinning dislocation for bending around x-axis [30] (a) and z-axis (b). Arrows indicate tension and compression side.

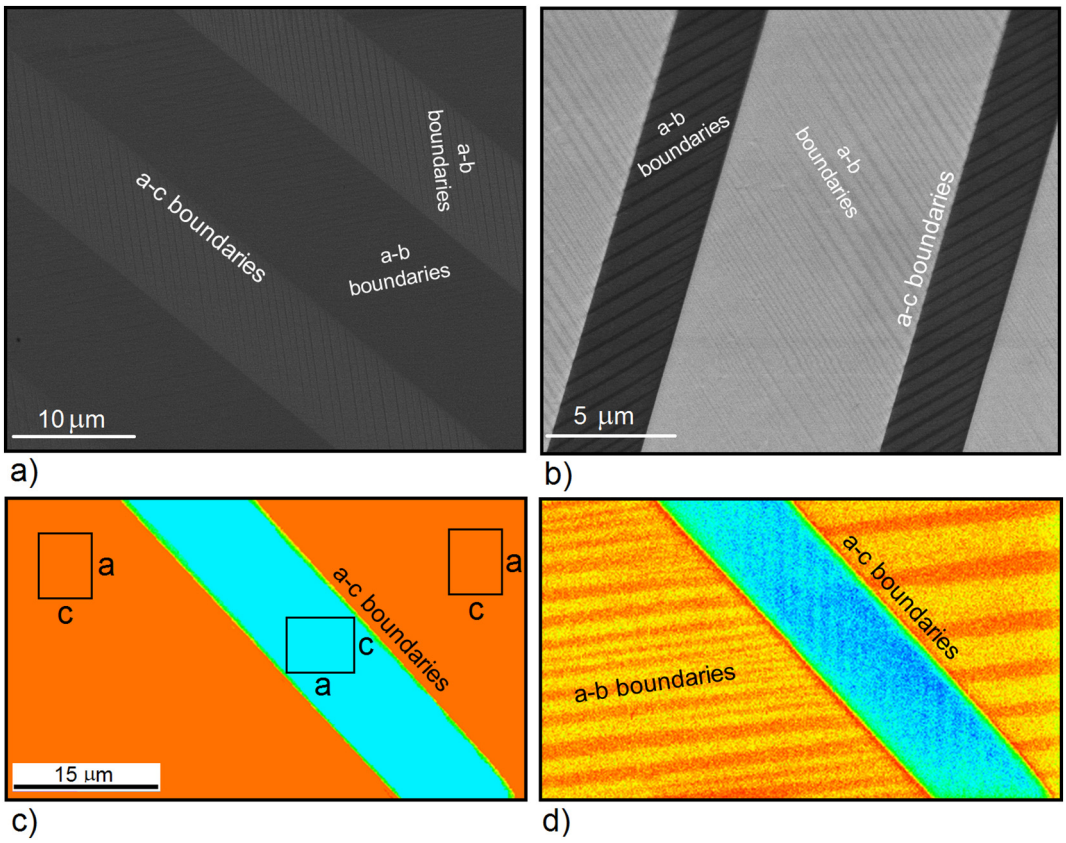

Fig. 7. BSE images showing *a-b* twins and *a-c* twins in the bent single crystals taken on the YZ (a) and XY (b) projections. EBSD maps done with conventional TSL (c) and dedicated Hough space software taken on the YZ projection (d).

[65-67] shall be construed as a situation where two twinning systems can intersect without inducing additional elastic stress fields in the material. This results in a specific low-energy morphology define by a characteristic zigzag pattern of *a-b* twin traces going continuously across the *a-c* interfaces. As a consequence, exactly the same volume fractions of the corresponding *a-b* variants on both sides of the *a-c* interface is obtained. Concurrently, both the *a-b* twins and the *a-c* twins are pinned (prevented from spontaneous motion) on the crossing points. Such a microstructure can be expected to appear in the unbent sample (Fig. 8a).

When the sample is bent (Fig. 8b), the *a-c* interfaces become inclined, and the geometric condition for compatible crossing becomes broken. While the *a-c* interfaces may remain macroscopically compatible (i.e., being planes providing compatible connection between the two a-b laminates under given bending stress), microscopically, the *a-b* laminates must undergo refinement to facilitate compatibility along the *a-c* interfaces. At least, such refinement might be expected for significantly inclined interfaces or pronounced jumps in *a-b* volume fractions. However, the real microstructure at each *a-c* interface in the bent sample is a result of energy balance between the macro-scale and micro-scale compatibility requirements. It seems to be most energetically favorable for the material to break the compatible crossings only at a certain number of interfaces, but keep it at the others, especially at those which do not incline when the sample is bent, Fig. 8. Hence, patterns of different levels of refinement of the *a-b* microstructure at neighboring *a-c* interfaces, as observed in Figs. 3b and 7d, can be expected.

The secondary effect of breaking the compatible connections at the inclined interfaces is the reduction of the characteristic lengths of the *a-b* twinning planes. In the unbent sample, continuous, undisturbed *a-b* twinning planes may run from one free surface of the crystal to another, changing their orientation by 90° any time they compatibly cross with the *a-c* twinning planes. In the bent sample, the continuity of the planes is broken, and the refined *a-b* laminates appear in regions bounded by pairs of planes being just tens of micrometers from each other (Fig. 8). From the theoretical models [65,68], it is known that the energy of such a constrained laminate is minimal if the width of the twins is proportional to square root of the length of the twins, in case that no branching appears. If the branching appears, the laminate can get coarser in its middle part, but significantly finer at the interfaces. In any case, the *a-b* laminate constrained between two near *a-c* twinning planes can be expected to exhibit significantly lower characteristic length-scale than the laminate spreading undisturbed over the whole sample (Fig. 8).

Nevertheless, although the above given theoretical considerations enable some insight into the mechanisms leading to twins rearrangement and refinement in the bent sample, they do not give any quantitative predictions, such specific twin thickness which leads to energy minimization or what are the critical levels of bending stress required for the rearrangement of the twin interfaces. Such an analysis falls beyond the scope of this paper, and would require accurate knowledge of the material parameters, such as the critical stress for motion of the *a-b* twins or the specific surface energy of the twin interfaces, which are both very hard to determine experimentally. Further theoretical analysis of the bent structures is therefore needed.

4. Conclusions

As a conclusion the paper underlines the importance of tapering of *a-c* twins and elastic change of lattice parameters as the main reasons for pseudoelastic effect in the bent 10M Ni-Mn-Ga single crystals. The plastic-elastic response can be explained by an equilibrium between the distance of the piled-up dislocations and twinning stress. Additionally, synchrotron radiation and electron backscatter diffraction have revealed that the tapering of *a-c* twin boundaries is inseparably linked

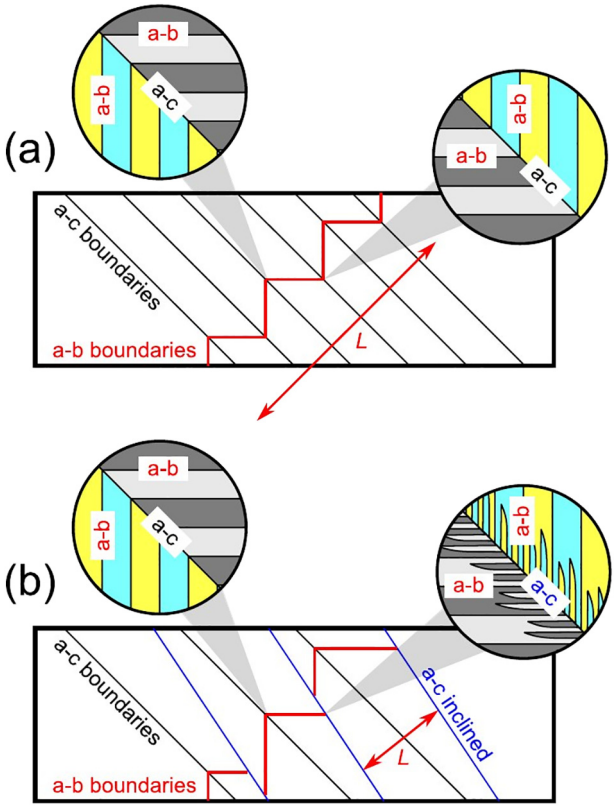

Fig. 8. Differences in microstructure in the unbent (a) and bent (b) single crystals with mixture of *a*-*b* and *a*-*c* twins seen on the YZ projection. (a) all twinning planes are crossing compatibly, and the characteristic length of the a-b interfaces *L* is given by the size of the crystal; (b) the compatible crossing is disturbed at the inclined interfaces, refinement of the *a*-*b* laminates appears at these interfaces via branching, and the length *L* is significantly reduced.

with interchange of *a* and *b*-variants or *a*-*b* lamination. The refinement and branching of *a*-*b* laminate can be understood on the base of the continuum mechanics of twin microstructure. Upon unloading the initial parallel twin configuration is recovered and the initial coarse configuration of the *a*-*b* boundaries is restored. As a result bending with a large bending angle in ferromagnetic Ni-Mn-Ga single crystals of desired functionality was obtained.

Credit author statement

R.C. SEM/EBSD and synch. experiments, evaluation, writing manuscript.
L.S. bending experiments.
H.S. theoretical modelling.
A.S. single crystal production.
N.S. synch. experiments.
T. T. mechanical tests.

Acknowledgement

The work was carried out within the project 2017/25/B/ST8/02524 of the National Science Centre of Poland. A part of this work was also financed by Juventus Plus Program, Project No. 0063/IP2/2015/73 of the Ministry of Science and Higher Education of Poland. This project has received funding from the European Union's Horizon 2020 research and innovation programme under grant agreement No 701867 – FUNMAH and from the Czech Science Foundation (Czech Republic) [grant number 17-00062S]. H. Seiner acknowledges R.D. James (University of Minnesota) for discussions and J. William Fulbright Commission (Prague) for support.

References

[1] C. Morin, Z. Moumni, W. Zaki, A constitutive model for shape memory alloys accounting for thermomechanical coupling, Int. J. Plast. 27 (5) (2011) 748–767, https://doi.org/10.1016/j.ijplas.2010.09.005.
[2] L. Straka, A. Soroka, H. Seiner, H. Hanninen, A. Sozinov, Temperature dependence of twinning stress of Type I and Type II twins in 10M modulated Ni-Mn-Ga martensite, Scripta Mater. 67 (2012) 25–28, https://doi.org/10.1016/j.scriptamat.2012.03.012.
[3] J. Wang, H. Sehitoglu, Twinning stress in shape memory alloys: theory and experiments, Acta Mater. 61 (2013) 6790–6801, https://doi.org/10.1016/j.actamat.2013.07.053.
[4] K. Haldar, D.C. Lagoudas, I. Karaman, Magnetic field-induced martensitic phase transformation in magnetic shape memory alloys: modeling and experiments, J. Mech. Phys. Solids. 69 (2014) 33–66, https://doi.org/10.1016/j.jmps.2014.04.011.
[5] B.T. Lester, T. Baxevanis, Y. Chemisky, D.C. Lagoudas, Review and perspectives: shape memory alloy composite systems, Acta Mech. 226 (12) (2015) 3907–3960, https://doi.org/10.1007/s00707-015-1433-0.
[6] P. Ranzieri, M. Campanini, S. Fabbrici, L. Nasi, F. Casoli, R. Cabassi, E. Buffagni, V. Grillo, C. Magen, F. Celegato, G. Barrera, P. Tiberto, F. Albertini, Achieving giant magnetically induced reorientation of martensitic variants in magnetic shape-memory Ni-Mn-Ga films by microstructure engineering, Adv. Mater. 27 (2015) 4760–4766, https://doi.org/10.1002/adma.201502072.
[7] D. Musiienko, L. Straka, L. Klimasa, A. Saren, A. Sozinov, O. Heczko, K. Ullakko, Giant magnetic-field-induced strain in Ni-Mn-Ga micropillars, Scripta Mater. 150 (2018) 173–176, https://doi.org/10.1016/j.scriptamat.2018.03.020.
[8] N. Zreihan, E. Faran, D. Shilo, The effect of loading rate on characteristics of type II twin boundary motion in Ni-Mn-Ga, Scripta Mater. 144 (2018) 44–47, https://doi.org/10.1016/j.scriptamat.2017.09.045.
[9] M. Acet, L. Manosa, A. Planes, Magnetic-field-induced effects in martensitic Heusler-based magnetic shape memory alloys in Handbook of Magnetic Materials, edited by K. H. J. Buschow (Elsevier, Amsterdam, 2011) Vol. 19 pp. 231 2011.
[10] S.J. Murray, M. Marrioni, S.M. Allen, R.C. O'Handley, 6% magnetic-field-induced strain by twin-boundary motion in ferromagnetic Ni-Mn-Ga, Appl. Phys. Lett. 77 (2000) 886–888, https://doi.org/10.1063/1.1306635.
[11] W. Zaki, An efficient implementation for a model of martensite reorientation in martensitic shape memory alloys under multiaxial nonproportional loading, Int. J. Plast. 37 (2012) 72–94, https://doi.org/10.1016/j.ijplas.2012.04.002.
[12] O. Heczko, V. Kopecky, A. Sozinov, L. Straka, Magnetic shape memory effect at 1.7 K, Appl. Phys. Lett. 103 (2013), 072405. https://doi.org/10.1063/1.4817941.
[13] A. Sozinov, N. Lanska, A. Soroka, W. Zou, 12% magnetic field-induced strain in Ni-Mn-Ga-based non-modulated martensite, Appl. Phys. Lett. 102 (2) (2013), 021902. https://doi.org/10.1063/1.4775677.
[14] E. Pagounis, R. Chulist, M.J. Szczerba, M. Laufenberg, Over 7% magnetic field-induced strain in a NiMnGa five-layered martensite, Appl. Phys. Lett. 105 (2014), 052405. https://doi.org/10.1063/1.4892633.
[15] S. Zhang, X. Chen, Z. Moumni, Y. He, Thermal effects on high-frequency magnetic-field-induced martensite reorientation in ferromagnetic *shape memory alloys*: an experimental and theoretical investigation, Int. J. Plast. 108 (2018) 1–20, https://doi.org/10.1016/j.ijplas.2018.04.008.
[16] S. Zhang, X. Chen, Z. Moumni, Y. He, Coexistence and compatibility of martensite reorientation and phase transformation in high-frequency magnetic-field-induced deformation of Ni-Mn-Ga single crystal, Int. J. Plast. 110 (2018) 110–122, https://doi.org/10.1016/j.ijplas.2018.06.010.
[17] H. Seiner, L. Straka, O. Heczko, A microstructural model of motion of macro-twin interfaces in Ni-Mn-Ga 10 M martensite, J. Mech. Phys. Sol. 64 (2014) 198–211, https://doi.org/10.1016/j.jmps.2013.11.004.
[18] E. Faran, D. Shilo, Implications of twinning kinetics on the frequency response in NiMnGa actuators, Appl. Phys. Lett. 100 (2012) 151901–151904, https://doi.org/10.1063/1.3702459.
[19] E. Faran, D. Shilo, The kinetic relation for twin wall motion in NiMnGa Part2, J. Mech. Phys. Solids. 61 (2013) 726–741, https://doi.org/10.1016/j.jmps.2012.11.004.
[20] O.Z. Pascan, Y.J. He, Z. Moumni, W.H. Zhang, Temperature rise of high-frequency martensite reorientation via type II twin boundary motion in NiMnGa ferromagnetic shape memory alloy, Scripta Mater. 104 (2015) 71–74, https://doi.org/10.1016/j.scriptamat.2015.04.006.
[21] O. Heczko, L. Klimša, J. Kopeček, Direct observation of ab twin laminate in monoclinic five-layered martensite of Ni-Mn-Ga magnetic shape memory single crystal, Scripta Mater. 131 (2017) 76–79, https://doi.org/10.1016/j.scriptamat.2017.01.010.
[22] R. Niemann, S. Fähler, Geometry of adaptive martensite in Ni-Mn- based Heusler alloys, J. Alloy. Comp. 703 (2017) 280–288, https://doi.org/10.1016/j.jallcom. 2017.01.189.
[23] R. Niemann, A. Backen, S. Kauffmann-Weiss, C. Behler, U.K. Rößler, H. Seiner, O. Heczko, K. Nielsch, L. Szultz, S. Fähler, Nucleation and growth of hierarchical martensite in epitaxial shape memory films, Acta Mater. 132 (2017) 327–334, https://doi.org/10.1016/j.actamat.2017.04.032.
[24] C.M. Wayman, Shape memory and related phenomena, Prog. Mater. Sci. 36 (1992) 203–224, https://doi.org/10.1016/0079-6425(92)90009-V.
[25] P.K. Purohit, K. Bhattachaya, On beams made of a phase-transforming material, Inter. J. Sol. Struct. 39 (2002) 3907, https://doi.org/10.1016/S0020-7683(02)00187-7.
[26] M. Chmielus, V.A. Chernenko, W.B. Knowlton, G. Kostorz, P. Müllner, Training, constraints and high-cycle magneto-mechanical properties of Ni-Mn-Ga magnetic shape memory alloys, Eur. Phys. J. Spec. Top. 158 (2008) 79–85, https://doi.org/10.1140/epjst/e2008-00657-3.
[27] P. Müllner, G. Kostorz, Microstructure of magnetic shape-memory alloys: between magnetoelasticity and magnetoplasticity, Mater. Sci. Forum 583 (2008) 43–65, https://doi.org/10.4028/www.scientific.net/MSF.583.43.

[28] L. Straka, H. Hänninen, N. Lanska, A. Sozinov, Twin interaction and large magnetoelasticity in Ni-Mn-Ga single crystals, J. Appl. Phys. 109 (2011), 063504. https://doi.org/10.1063/1.3552292.

[29] R. Chulist, W. Skrotzki, C.-G. Oertel, A. Böhm, M. Pötschke, Change in microstructure during training of a $Ni_{50}Mn_{29}Ga_{21}$ bicrystal, Scripta Mater. 63 (2010) 548–551, https://doi.org/10.1016/j.scriptamat.2010.05.028.

[30] R. Chulist, A. Sozinov, L. Straka, N. Lanska, A. Soroka, T. Lippmann, C.G. Oertel, W. Skrotzki, Diffraction study of bending-induced polysynthetic twins in 10M modulated Ni-Mn-Ga martensite, J. Appl. Phys. 112 (2012), 063517. https://doi.org/10.1063/1.4754017.

[31] R. Chulist, L. Straka, A. Sozinov, T. Tokarski, W. Skrotzki, Branched needle microstructure in Ni-Mn-Ga 10M martensite: EBSD study, Acta Mater. 128 (2017) 113–119, https://doi.org/10.1016/j.actamat.2017.02.024.

[32] R. Mirzaeifar, R. DesRoches, A. Yavari, K. Gall, On superelastic bending of shape memory alloy beams, Int. J. Solids Struct. 50 (2013) 1664–1680, https://doi.org/10.1016/j.ijsolstr.2013.01.035.

[33] F. Auricchio, E. Bonetti, G. Scalet, F. Ubertini, Theoretical and numerical modeling of shape memory alloys accounting for multiple phase transformations and martensite reorientation, Int. J. Plast. 59 (2014) 30–54, https://doi.org/10.1016/j.ijplas.2014.03.008.

[34] Y. Xin, Y. Zhou, Martensitic transformation and mechanical properties of NiMnGaV high-temperature shape memory alloys, Intermetal. 73 (2016) 50–57, https://doi.org/10.1016/j.intermet.2016.03.005.

[35] C. Witherspoon, P.Q. Zheng, M. Chmielus, S.C. Vogel, D.C. Dunand, P. Müllner, Texture and training of magnetic shape memory foam, Acta Mater. 61 (2013) 2113–2120, https://doi.org/10.1016/j.actamat.2012.12.032.

[36] E.E. Timofeeva, E.Yu. Panchenko, M.V. Pichkaleva, A.I. Tagiltsev, Yu.I. Chumlyakov, The effect of stress-induced martensite ageing on the two-way shape memory effect in Ni53Mn25Ga22 single crystals, Mater. Lett. 228 (2018) 490–492, https://doi.org/10.1016/j.matlet.2018.06.086.

[37] J. Feuchtwanger, E. Seif, P. Sratongon, H. Hosoda, V.A. Chernenko, Vibration damping of Ni-Mn-Ga/silicone composites, Scripta Mater. 146 (2018) 9–12, https://doi.org/10.1016/j.scriptamat.2017.10.028.

[38] R. Chulist, L. Straka, A. Sozinov, T. Lippmann, W. Skrotzki, Modulation reorientation in 10M Ni-Mn-Ga martensite, Scripta Mater. 68 (2013) 647–671.

[39] N.V. Viet, W. Zaki, R. Umer, Analytical model of functionally graded material/shape memory alloy composite cantilever beam under bending, Comp. Struct. 203 (2018) 764–776, https://doi.org/10.1016/j.compstruct.2018.07.041.

[40] B.S. Shariat, Y. Liu, S. Bakhtiari, Modelling and experimental investigation of geometrically graded *shape memory alloys* with parallel design configuration, J. Alloy. Comp. (2019)https://doi.org/10.1016/j.jallcom.2019.03.119.

[41] Y.J. Kim, C.H. Lee, J.H. Kim, J.H. Lim, Numerical modeling of *shape memory alloy* plates considering tension/compression asymmetry and its verification under pure *bending*, Int. J. Solids Struct. 136 (2018) 77–88, https://doi.org/10.1016/j.ijsolstr.2017.12.004.

[42] Y. Zhao, M. Kang, J. Xue, J. Ju, M. Wang, S. Wang, Y. Zhang, M. Vázquez, H. Gao, J. Wang, Strain-magnetization effect in superelastic Ni-Mn-Ga microfiber, Scripta Mater. 162 (2019) 397–401, https://doi.org/10.1016/j.scriptamat.2018.12.002.

[43] A. Eshghinejad, M. Elahinia, Exact solution for bending of shape memory alloy beams, Mech. Adv. Mater. Struct. (2011) 22, https://doi.org/10.1115/SMASIS2011-5151.

[44] K. Otsuka, H. Sakamoto, K. Shimizu, A new type of pseudoelasticity in single variant twinned martensites, Scripta Metall. 11 (1977) 41–46, https://doi.org/10.1016/0036-9748(77)90010-2.

[45] H.D. Chopra, C. Bailly, M. Wuttig, Domain structures in bent In-22.5at.%Tl polydomain crystals, Acta Mater. 44 (1996) 747–751, https://doi.org/10.1016/1359-6454(95)00183-2.

[46] Y. Ganor, T. Dumitrica, F. Feng, R.D. James, Zig-zag twins and helical phase transformations, Phil. Tran. R. Soc. A. 374 (2016), 20150208. https://doi.org/10.1098/rsta.2015.0208.

[47] R. Chulist, M. Faryna, M.J. Szczerba, Orientation relationship between austenite and non-modulated martensite in Ni-Mn-Ga single crystals, Acta Mater. 103 (24) (2016) 836–843, https://doi.org/10.1016/j.actamat.2015.11.007.

[48] R. Chulist, M. Faryna, M.J. Szczerba, Asymmetric distribution of martensitic variants in non-modulated NiMnGa single crystals, J. Mat. Scien. 51 (24) (2016), 10943. https://doi.org/10.1007/s10853-016-0306-9.

[49] P. Czaja, M.J. Szczerba, R. Chulist, M. Bałanda, J. Przewoźnik, Y.I. Chumlyakov, N. Schell, Cz. Kapusta, W. Maziarz, Martensitic transition, structure and magnetic anisotropy of martensite in Ni-Mn-Sn single crystal, Acta Mater. 118 (2016) 213–220, https://doi.org/10.1016/j.actamat.2016.07.059.

[50] P. Czaja, R. Chulist, T. Tokarski, T. Czeppe, Y.I. Chumlyakov, E. Cesari, Superelastic behavior of a metamagnetic Ni-Mn-Sn single crystal, J. Mater. Sci. 53 (2018) 10383–10395, https://doi.org/10.1007/s10853-018-2289-1.

[51] L. Zhou, M.M. Schneider, A. Giri, K. Cho, Y. Sohn, Microstructural and crystallographic characteristics of modulated martensite, non-modulated martensite, and pre-martensitic tweed austenite in Ni-Mn-Ga alloys, Acta Mater. 134 (2017) 93–103, https://doi.org/10.1016/j.actamat.2017.05.050.

[52] R. Chulist, P. Czaja, T. Tokarski, I. Kuksgauzen, Y.I. Chumlyakov, Orthogonal shear process in Ni-Mn-Sn single crystal, Int. J. Plast. 114 (2019) 63–71, https://doi.org/10.1016/j.ijplas.2018.10.009.

[53] D.Y. Cong, Y.D. Zhang, C. Esling, Y.D. Wang, J.S. Lecomte, X. Zhao, L. Zuo, Microstructural and crystallographic characteristics of interpenetrating and non-interpenetrating multiply twinned nanostructure in a Ni-Mn-Ga ferromagnetic shape memory alloy, Acta Mater. 59 (2011) 7070–7081, https://doi.org/10.1016/j.actamat.2011.07.062.

[54] Z.B. Li, Y.D. Zhang, C. Esling, X. Zhao, L. Zuo, Determination of the orientation relationship between austenite and incommensurate 7M modulated martensite in Ni-Mn-Ga alloys, Acta Mater. 59 (2011) 2762–2772, https://doi.org/10.1016/j.actamat.2011.01.015.

[55] Z.B. Li, N. Xu, Y.D. Zhang, C. Esling, J.M. Raulot, X. Zhao, L. Zuo, Composition-dependent ground state of martensite in Ni–Mn–Ga alloys, Acta Mater. 61 (2016) 3858–3865, https://doi.org/10.1016/j.actamat.2013.03.024.

[56] Y. Liu, I. Karaman, H. Wang, X. Zhang, Two types of martensitic phase transformations in magnetic shape memory alloys by in-situ nanoindentation studies, Adv. Mater. 26 (2014) 3893–3898, https://doi.org/10.1002/adma.201400217.

[57] B. Muntifering, R.C. Pond, L. Kovarik, N.D. Browning, P. Müllner, Intra-variant substructure in Ni-Mn-Ga martensite: conjugation boundaries, Acta Mater. 71 (2014) 255–263, https://doi.org/10.1016/j.actamat.2014.03.018.

[58] B. Muntifering, L. Kovarik, N.D. Browning, R.C. Pond, W.B. Knowlton, P. Müllner, Stress-assisted removal of conjugation boundaries in nonmodulated Ni-Mn-Ga by coordinated secondary twinning, J. Mat. Sci. 51 (2016) 457–466, https://doi.org/10.1007/s10853-015-9236-1.

[59] R.I. Barabash, O.M. Barabash, D. Popov, G. Shen, C. Park, W. Yang, Multiscale twin hierarchy in NiMnGa shape memory alloys with Fe and Cu, Acta Mater. 87 (2015) 344–349, https://doi.org/10.1016/j.actamat.2015.01.010.

[60] S. Ouyang, Y.Q. Yang, M. Han, Z.H. Xia, B. Huang, X. Luo, G.M. Zhao, W. Zhang, Twin relationships between nanotwins inside A-C type variant pair in Ni-Mn-Ga alloy, Acta Mater. 84 (2015) 484–496, https://doi.org/10.1016/j.actamat.2014.11.001.

[61] Y. Dai, L. Hou, Y. Fautrelle, Z. Li, C. Esling, Z. Ren, X. Li, Detwinning process of martensite in Ni58Mn25Ga17 as a high temperature shape memory alloy under uniaxial compression, Int. J. Plast. 103 (2018) 203–213, https://doi.org/10.1016/j.ijplas. 2018.01.013.

[62] Y. Dai, L. Hou, Y. Fautrelle, Z. Li, C. Esling, Z. Ren, X. Li, Martensitic transformation and detwinning in directionally solidified two-phase Ni-Mn-Ga alloys under uniaxial compression, J. Alloy. Comp. 722 (2017) 721–728, https://doi.org/10.1016/j.jallcom.2017.06.129.

[63] S. Ozdemir Kart, T. Cagin, Elastic properties of Ni2MnGa from first-principles calculations, J. Alloy. Comp. 508 (2010) 177–183, https://doi.org/10.1016/j.jallcom.2010.08.039.

[64] R.V. Kohn, S. Müller, Branching of twins near an austenite-twinned martensite interface, Phil. Mag. 66 (1992) 697–715, https://doi.org/10.1080/01418619208201585.

[65] J.M. Ball, R.D. James, Fine phase mixtures as minimizers of energy, Arch. Ration. Mech. Anal. 100 (1987) 13–52, https://doi.org/10.1007/BF00281246.

[66] J.W. Christian, S. Mahajan, Deformation twinning, Prog. Mater. Sci. 39 (1995) 1–157, https://doi.org/10.1016/0079-6425(94)00007-7.

[67] K. Bhattacharya, Microstructure of Martensite: Why it Forms and how it Gives Rise to the Shape-memory Effect, Oxford University Press, New York, 2003.

[68] R.V. Kohn, S. Müller, Surface energy and microstructure in coherent phase transitions, Commun. Pure Appl. Math. 47 (1994) 405–435, https://doi.org/10.1002/cpa.3160470402.